Nitrogen and phosphorus adsorption in aqueous solutions by humic acids from weathered coal: isotherm, kinetics and thermodynamic analysis

Dan Liu, Zhanbin Huang, Shuhui Men, Zhen Huang and Chunrong Wang

ABSTRACT

The aim of this study was to reveal the mechanism of nitrogen and phosphorus adsorption by humic acids (HAs). HAs were extracted from weathered coal and used as adsorbents of urea-N and phosphate-P in water. The effect of different factors was considered, such as the initial concentration of urea-N and phosphate-P, temperature, and pH. The surface characteristics of the HAs were analyzed by X-ray diffraction, scanning electron microscopy, energy dispersive X-ray spectroscopy, and Fourier transform infrared spectrometry. The results of batch adsorption experiments showed high effectiveness for nitrogen adsorption, the kinetics fitted with the pseudo-second-order model, and the isotherm followed the Langmuir model. For phosphorus adsorption, the data fitted well with the Weber and Morris model and the adsorption isotherms followed both the Langmuir and Freundlich isotherm models. The experimental results indicated that the adsorption behavior of HAs was both an endothermic and spontaneous process. These findings can be used as a reference for the mitigation of non-point source pollution and the application of fertilizer in agriculture.

Key words | adsorption, humic acids, nitrogen, phosphorus, weathered coal

Dan Liu
Zhanbin Huang (corresponding author)
Shuhui Men
Zhen Huang
Chunrong Wang
School of Chemical and Environmental Engineering,
China University of Mining and Technology (Beijing),
Beijing 100083,
China
E-mail: *108742@cumtb.edu.cn*

Zhen Huang
Environmental Engineering Program, Department of Civil Engineering,
Auburn University,
Auburn, Alabama 36849,
USA

INTRODUCTION

Nitrogen and phosphorus are the main nutrients in aquatic systems (Huang *et al.* 2017). However, excessive loading of nitrogen and phosphorus will lead to eutrophication and substantial environmental damage (Dodd & Sharpley 2015; Ma *et al.* 2016). Since the 1960s, due to the increasing human population and socio-economic development, the use of nitrogen and phosphorus fertilizers has become much more widespread, demonstrated by a nine-fold increase in nitrogen application rates and a three-fold increase in phosphorus application rates (Leon & Kohyama 2017). Massive discharges of nitrogen and phosphorus are regarded as the primary reason for the eutrophication of groundwater. Therefore, the control of nitrogen and phosphorus is key to mitigating eutrophication and improving environmental sustainability (Yang *et al.* 2017).

In order to reduce the concentrations of nitrogen and phosphorus in eutrophic water bodies and raise the usage efficiency ratio of chemical fertilizer, many measures have been taken, such as deep placement (Zhang *et al.* 2018a), crop rotation, controlled-release fertilization, nutrient-balanced fertilization, and integrated management (Wang *et al.* 2018). However, these measures require greater money and labor inputs; thus, cheaper and more efficient technologies are required. Adsorption, which is an eco-friendly and economically feasible alternative, has received growing attention in recent years (Derylo-Marczewska *et al.* 2019; Liu *et al.* 2019). Common adsorbents include zeolite (Ji *et al.* 2013; He *et al.* 2017), boehmite (Qian *et al.* 2017), and fly ash (Uğurlu & Karaoğlu 2011). The availability of adsorbents depends on their adsorption efficiency, cost, and regeneration and reuse potential (Kuśmierek *et al.* 2016).

Humic acids (HAs) are natural organic macromolecular compounds that originate from complex biochemical transformations of plant and animal residues and are the primary component of soil organic matter (Canellas *et al.* 2015). HAs contain aromatic rings and conjugated double bonds and are rich in functional groups such as alkyl, carbohydrate, hydroxyl, aromatic, and carboxyl, which are closely related to their complexation properties and adsorption capacity (Ma *et al.* 2018). Therefore, HAs have significant effects on the aggregation, aeration, and water-holding capacity of soil (Zhang *et al.* 2019). Furthermore, organic

doi: 10.2166/wst.2019.218

complex fertilizers made with HAs and chemical fertilizers exhibit long-lasting fertilization efficacy (Zhao *et al.* 2016).

Weathered coal is one of main sources of HAs and has been widely used as a fertilizer and soil conditioner (Krumins *et al.* 2017). In China, weathered coal reserves are abundant and total approximately 100 billion tons (Zhang *et al.* 2017). As a highly effective and low-cost material, HAs have already been used for treating various organic contaminants (Zhang *et al.* 2012) and heavy metals (Shaker & Albishri 2014) in recent decades. However, the characteristics and mechanisms of nitrogen and phosphorus removal by HAs extracted from weathered coal have not previously been reported.

In this study, HAs derived from weathered coal were used as adsorbents and urea-N and phosphate-P fertilizers were used as adsorbates. To determine the optimal removal conditions, the effects of different factors such as initial pollutant concentration, temperature, and pH were considered. The adsorption mechanism was analyzed using various adsorption kinetics models and isotherm models. In addition, the adsorption thermodynamics of nitrogen and phosphorus on HAs were also investigated. The surface characteristics of HAs and the mechanism of humic acid and chemical fertilizer interactions were explored by X-ray diffraction (XRD), scanning electron microscopy (SEM), energy dispersive X-ray spectroscopy (EDS), and Fourier transform infrared spectrometer (FTIR). This study can be used for the mitigation of non-point source pollution. Furthermore, because HAs after adsorption have great potential as organic-inorganic compound fertilizers, this research has important applications for fertilizer use in agriculture.

MATERIALS AND METHODS

Chemicals and materials

Weathered coal (200 mesh (74 μm)) was obtained from Beijing Aojia Fertilizer Co. Ltd (Beijing, China). The nitrogen and phosphate fertilizers used in the experiment were urea ($CO(NH_2)_2$) and potassium phosphate monobasic (KH_2PO_4), respectively. $CO(NH_2)_2$) and KH_2PO_4 were purchased from Sinopharm Group Co. Ltd (Shanghai, China). All chemicals used for the experiment were of analytical grade, and deionized water was used to prepare the solutions.

Batch adsorption experiments

Weathered coal was spread on an enamel dish and exposed to air at room temperature (25 °C) for a defined period of time to advance natural weathering. Then, the weathered coal was leached in deionized water and stirred for 48 hours. After leaching, the solid residue was washed with deionized water several times, collected by centrifugation, and dried in an oven at 40 °C. The particles were sieved with a 200-mesh sieve to obtain the HA particles used in the experiments.

Batch adsorption experiments were conducted to investigate urea-N and phosphate-P adsorption behavior on HAs. Batch adsorption was performed in a set of 50-mL polypropylene plastic tubes containing 0.5 g of HA solids, 30 mL of 200 mg N/L (or 150 mg P/L), 0.01 mol/L $CaCl_2$, and a suitable amount of trichloromethane (to inhibit microbial activity). These tubes were capped and placed in an incubator shaker (HZQ-F100) for 60 hours at 25 °C. After being shaken, the solution was separated from the HAs by centrifugation for 10 min at 4,000 rpm and filtered through a 0.45-μm PTFE filter. To investigate the adsorption kinetics, the concentrations of urea-N and phosphate-P were measured at different times from 0 hours to 48 hours (0.5, 1, 2, 5, 9, 15, 24, 34, and 48 hours). To investigate the adsorption isotherms, the adsorption experiments were conducted by varying the initial concentration of the urea-N and phosphate-P solution (0, 30, 90, 150, 300, 600, and 1,200 mg N/L and 0, 40, 120, 200, 400, 800, and 1,600 mg P/L). To determine the thermodynamic properties and the effect of temperature on these adsorption process, the adsorption isotherms were determined at four different temperatures (288, 298, 308, and 318 K). The effect of initial pH on the adsorption process was investigated by adjusting the pH of the urea-N and phosphate-P solution from 3 to 11 (3, 5, 7, 9, and 11). The pH was adjusted with dilute HCl and NaOH at appropriate concentrations. All experiments were conducted in triplicate.

Analytical methods

The XRD patterns of the HAs were obtained using a wide-angle X-ray diffractometer (D8 Advance, Bruker, Germany). The morphology and elemental maps of the HAs were measured by a scanning electron microscope (SU8010, Hitachi, Japan) equipped with an energy dispersive spectroscope. The surface functional groups were analyzed with a Fourier transform infrared spectroscope (Spectrum One, Perkin Elmer, USA). Spectrophotometry was used to measure the nitrogen and phosphate concentrations with an ultraviolet-visible (UV–vis) spectrophotometer (UV-1100, China). The nitrogen concentration was determined by the alkaline potassium persulfate digestion UV spectrophotometric method, and the phosphate concentration was analyzed by the molybdenum blue method.

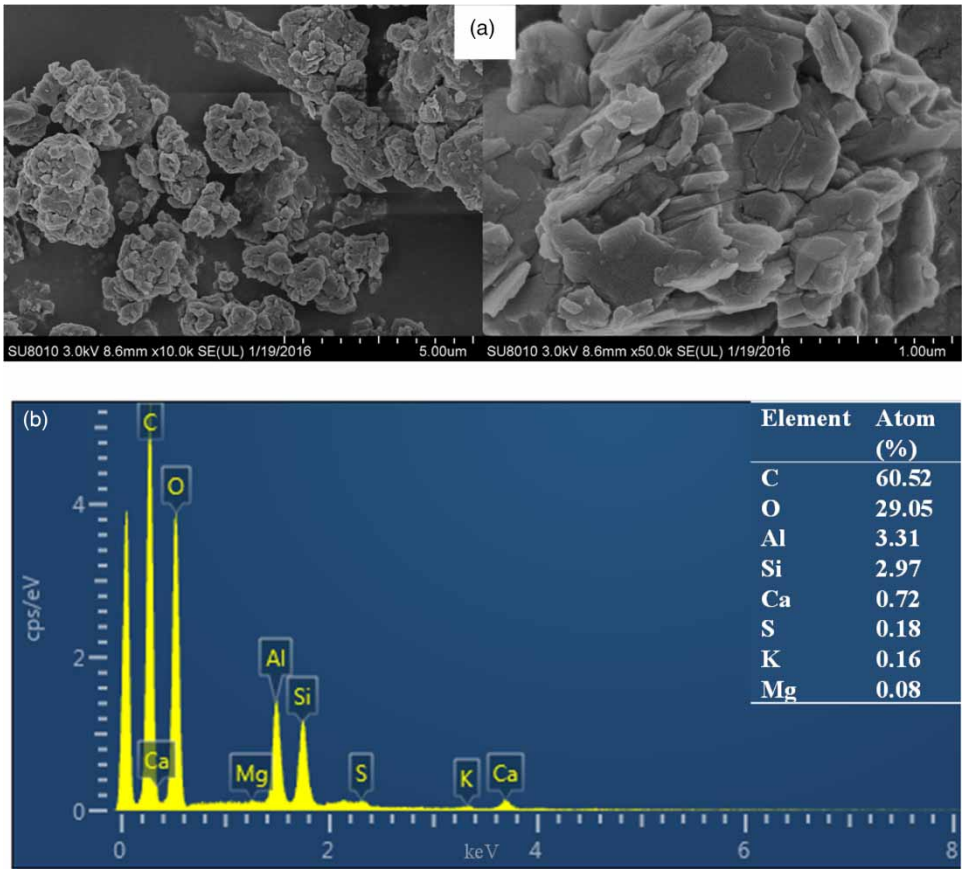

Figure 1 | SEM micrographs (a) and EDS analysis (b) of the humic acids.

RESULTS AND DISCUSSION

Surface characteristics of humic acids

The morphology of the HAs was analyzed using SEM micrographs at different magnifications (Figure 1(a)). These images show that the HAs are composed of irregular laminar particle aggregates. HA composition, which was characterized by EDS (Figure 1(b)), indicates that carbon (C), oxygen (O), aluminum (Al), and silicon (Si) are the major elements. Moreover, a small amount of calcium (Ca), sulfur (S), potassium (K), and magnesium (Mg) is observed. According to the atomic ratios of C, O, Al Si, it can be inferred that organic compounds are the main ingredients of the HAs. However, the presence of aluminosilicate cannot be ignored.

To further characterize the structural properties of the HAs and the crystalline phases of the aluminosilicate within, XRD patterns of the HAs were determined (Figure 2). The diffraction lines of the HAs can be readily indexed to kaolinite ($Al_4(OH)_8(Si_4O_{10})$, JCPDS: 78-2109). The diffraction peaks at 2θ of 12.51°, 21.45°, 25.11°, 35.14°, 38.58°, 45.69°, and 62.47° correspond to the (001), (-1-11), (002), (130), (1–31), (1–32), and (−331) planes of kaolinite, respectively (Wang *et al.* 2016). The other diffraction reflection at 2θ of

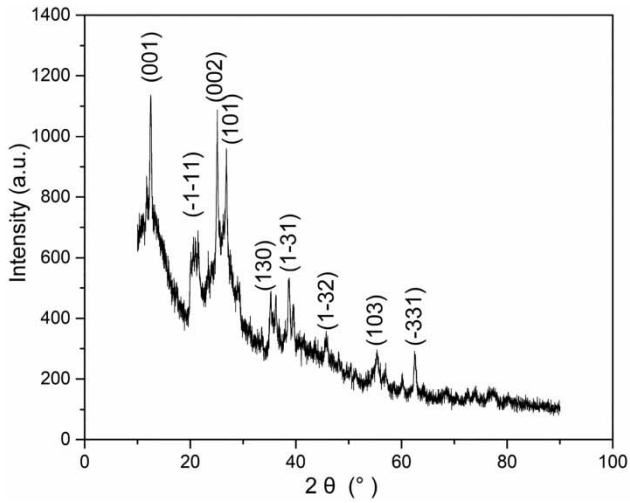

Figure 2 | XRD pattern of the humic acids.

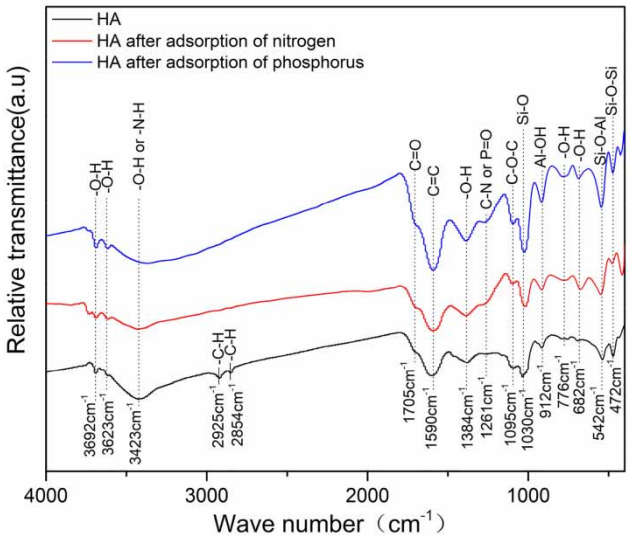

Figure 3 | The FT-IR spectrum of humic acids.

26.80° and 55.34° correspond to the (101) and (103) planes of quartz (SiO_2, JCPDS: 83-2465). XRD analysis confirmed that the HAs mainly contain organic compounds and kaolinite. Moreover, kaolinite provides a stable structural support for the organic compounds.

HAs before and after adsorption are illustrated by FTIR spectra in Figure 3 in order to analyze the functional groups in the materials. The peak at 3,692 cm^{-1} is attributed to the stretching vibrations of the surface hydroxyl groups (O-H) and the peak at 3,623 cm^{-1} is assigned to the inner hydroxyl groups. The band at 3,423 cm^{-1} is associated with the N-H stretching vibration or O-H stretching vibration (Zhang *et al.* 2018b). In addition, the absorption peaks at 2,925 cm^{-1} and 2,854 cm^{-1} belong to asymmetric and symmetric vibrations of $-CH_2$, indicating that the HAs contain a small amount of aliphatic hydrocarbons (Misra *et al.* 2018). Moreover, HA spectra reveal the characteristic bands of carboxylic acids at 1,705 cm^{-1} (C = O stretching vibration) and aromatics at 1,590 cm^{-1} (C = C stretching vibration) (Qie *et al.* 2018). The broad band at 1,384 cm^{-1} is attributed to the O-H deformation vibration of the hydroxyl groups from phenols. The peaks at 1,030 cm^{-1} (Si-O), 912 cm^{-1} (Al-OH), 542 cm^{-1} (Si-O-Al) and 472 cm^{-1} (Si-O-Si) are typical bands of kaolinite, illustrating the presence of kaolinite in the HAs. The low intensity band around 1,095 cm^{-1} mainly reflects the C-O-C stretching vibration from ethers. Furthermore, the appearance of new peaks at 1,261 cm^{-1} after adsorption could be attributed to the stretching vibration of C-N or P = O. The slight shift of the band around 1,705 cm^{-1} after adsorption indicates that the -COOH groups on the HAs are probably involved in the adsorption interaction via H-bonding.

Adsorption kinetics

To study the adsorption kinetics of nitrogen and phosphorus by the HAs, pseudo-first-order, pseudo-second-order, Elovich, and Weber and Morris intra-particle diffusion kinetic models were employed.

The pseudo-first-order kinetic model is as follows (Lagergren 1898):

$$\ln(q_e - q_t) = \ln q_e - k_1 t \quad (1)$$

where q_e ($mg \cdot g^{-1}$) and q_t ($mg \cdot g^{-1}$) represent the amount of adsorbate (urea-N or phosphate-P) adsorbed by the HAs after equilibrium at time t (h), and k_1 represents the pseudo first-order adsorption rate constant (h^{-1}). The slope from the linear plot of $\ln(q_e - q_t)$ versus t indicates the value of k_1.

The pseudo-second-order kinetic model is as follows:

$$\frac{t}{q_t} = \frac{1}{k_2 q_e^2} + \frac{t}{q_e} \quad (2)$$

where k_2 ($g \cdot mg^{-1} \cdot h^{-1}$) is the pseudo-second-order adsorption rate constant. The values of k_2 and q_e can be calculated from the slope and intercept of the plot of t/q_t versus t.

The Elovich kinetic model is as follows:

$$q_t = \frac{1}{\beta}\ln(\alpha\beta) + \frac{1}{\beta}\ln t \quad (3)$$

where α ($g \cdot mg^{-1} \cdot h^{-1}$) and β ($g \cdot mg^{-1}$) are the Elovich constants. The constants α and β can be determined from the plot of q_t versus lnt.

The Weber and Morris intra-particle diffusion kinetic model is as follows (Weber & Morris 1963):

$$q_t = k_I t^{0.5} + C \quad (4)$$

where k_I ($mg \cdot g^{-1} \cdot h^{-0.5}$) is the intra-particle diffusion rate constant and C ($mg \cdot g^{-1}$) is a constant that incorporates the thickness of the boundary layer. The slope and intercept values of the plot of q_t versus $t^{0.5}$ give the value of k_I and C, respectively.

The adsorption kinetics data of nitrogen and phosphorus adsorption on the HAs and the four fitting kinetic models are shown in Figure 4. At first, the adsorption rate is fast. It then

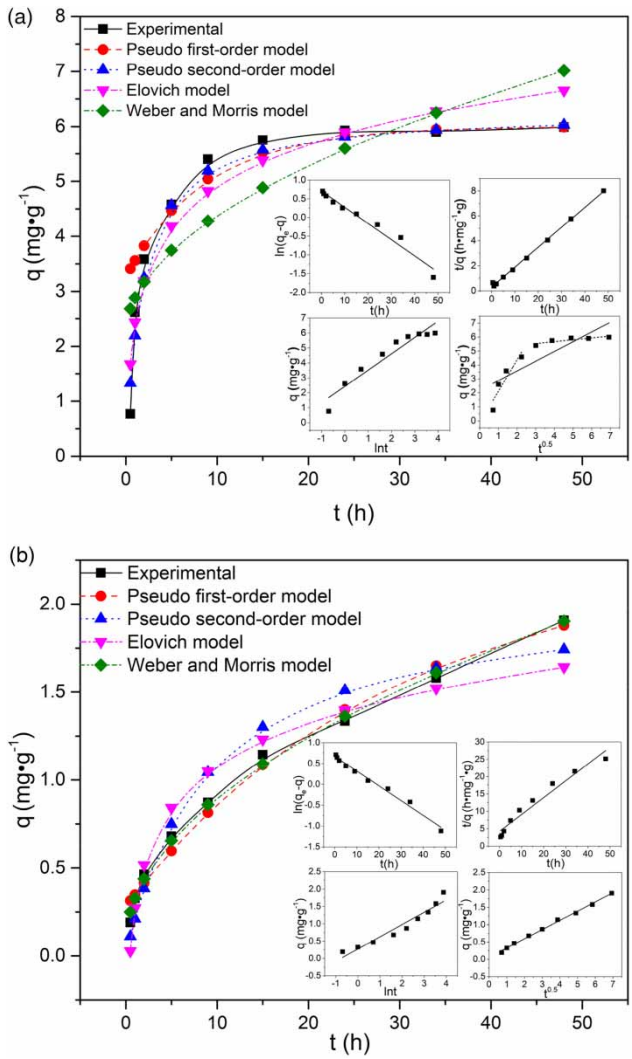

Figure 4 | Adsorption kinetic model of nitrogen (a) and phosphorus (b) on the humic acids at 298 K.

slows before gradually reaching equilibrium. The adsorption rate is affected by the concentration gradient of the adsorbate between the adsorbent and solution. The fast initial adsorption rate might be due to the high concentration gradient and sufficient initially available vacant sites on the surface (Zhu *et al.* 2018). As the sites become covered, the urea-N and phosphate-P adsorbed on the surfaces of the HAs may then diffuse into the interlayer structure of the HAs at a slow rate. As the percentage composition of nitrogen and phosphorus increases on the surface of the HAs, the diffusion resistance increases, leading to a further decrease in the intra-particle diffusion rate, then eventual equilibrium. A comparison between the adsorption capacities of HAs on nitrogen (6.034 mg $N{\bullet}g^{-1}$ at 60 hours) and phosphorus (2.234 mg $P{\bullet}g^{-1}$ at 60 hours) indicates that HAs provide more sites for nitrogen adsorption than for phosphorus adsorption. The equations of the four kinetic models and the values of their corresponding parameters are shown in Table 1.

The nitrogen adsorption capacity increases with time, reaching 4.58 mg $N{\bullet}g^{-1}$ (50.9% nitrogen removal rate) at 5 hours and 5.99 mg $N{\bullet}g^{-1}$ (66.5% nitrogen removal rate) at 48 hours. As seen from Table 1, the pseudo-second-order kinetic model best simulates the kinetic adsorption process with a higher correlation coefficient ($R^2 = 0.998$) than the other three models. In addition, $q_{e\text{-}cal}$ (6.262 mg $N{\bullet}g^{-1}$) calculated from the pseudo-second-order plot fits well with the $q_{e\text{-}exp}$ (6.034 mg $N{\bullet}g^{-1}$) value obtained in the experiments. This indicates that the adsorption between urea-N and HAs is dominated by the absorption sites on the surfaces of HAs rather than the urea-N concentration in the solution. (Zhang *et al.* 2012) Furthermore, the two-linearity plot of the intra-particle diffusion kinetic model indicates that film diffusion and intra-particle diffusion occur during the nitrogen adsorption process on HAs.

The phosphorus adsorption capacity reaches 0.68 mg $P{\bullet}g^{-1}$ (7.3% phosphorus removal rate) at 5 hours and 1.91 mg $P{\bullet}g^{-1}$ (21.2% phosphorus removal rate) at 48 hours. Although the four models adequately fit the kinetics data of phosphorus adsorption on HAs, the Weber and Morris intra-particle diffusion kinetic model, with an R^2 over 0.99, shows a better fit than the other models. The single straight line of the Weber and Morris intra-particle diffusion kinetic model indicates that phosphorus adsorption on HAs is dominated by intra-particle diffusion. However, the intra-particle diffusion plot does not pass through the origin (the value of C is larger than 0), indicating that intra-particle diffusion is not the only rate-limiting step (Konggidinata *et al.* 2017). These results show that the adsorption process of phosphorus on HAs is governed by more than one adsorption mechanism and might be a complex process that includes both intra-particle diffusion and surface adsorption.

Equilibrium adsorption isotherms

The adsorption capacity of urea-N and phosphate-P on the HAs can be described by adsorption isotherms. Here, three isotherm models (Langmuir, Freundlich, and Temkin) were used to investigate the equilibrium characteristics.

The Langmuir isotherm is as follows (Langmuir 1918):

$$\frac{C_e}{q_e} = \frac{C_e}{q_m} + \frac{1}{K_L q_m} \tag{5}$$

where C_e ($mg{\bullet}L^{-1}$) is the equilibrium concentration of the adsorbate (nitrogen or phosphorus), q_e ($mg{\bullet}g^{-1}$) represents

Table 1 | Fitting parameters for the kinetic models calculated from experimental data

Adsorbates	Pseudo-first-order model				Pseudo-second-order model				Elovich model				Weber and Morris model			
	$q_{e,exp}$ (mg•g^{-1})	k_1 (h^{-1})	$q_{e,cal}$ (mg•g^{-1})	R^2	$q_{e,exp}$ (mg•g^{-1})	k_2 (mg•g^{-1}•h^{-1})	$q_{e,cal}$ (mg•g^{-1})	R^2	α (g•mg^{-1}•h^{-1})	β (g•mg^{-1})	R^2	C (mg•g^{-1})	k_p (mg•g^{-1}•h$^{-0.5}$)	R^2
N	6.034	0.117	2.745	0.925	6.034	0.086	6.262	0.998	10.128	0.917	0.918	2.188	0.697	0.707
P	2.234	0.036	1.953	0.978	2.234	0.056	2.060	0.952	0.764	2.826	0.929	0.062	0.266	0.997

the adsorption capacity of the adsorbate (nitrogen or phosphorus) adsorbed by the HAs at equilibrium, K_L (L•mg^{-1}) is the Langmuir equilibrium constant, and q_m (mg•g^{-1}) is the maximum adsorption capacity. The related parameters of the Langmuir isotherm were obtained from the intercept and slope values of the plot of C_e/q_e versus C_e.

The Freundlich isotherm is as follows (Freundlich 1906):

$$\ln q_e = \ln K_F + \frac{1}{n}\ln C_e \tag{6}$$

where K_F [(mg•g^{-1})(L•mg^{-1})$^{1/n}$] is the Freundlich equilibrium constant and n is a constant that describes the adsorption intensity. The corresponding parameters of the Freundlich isotherm were determined from the intercept and slope values of the plot of $\ln q_e$ versus $\ln C_e$.

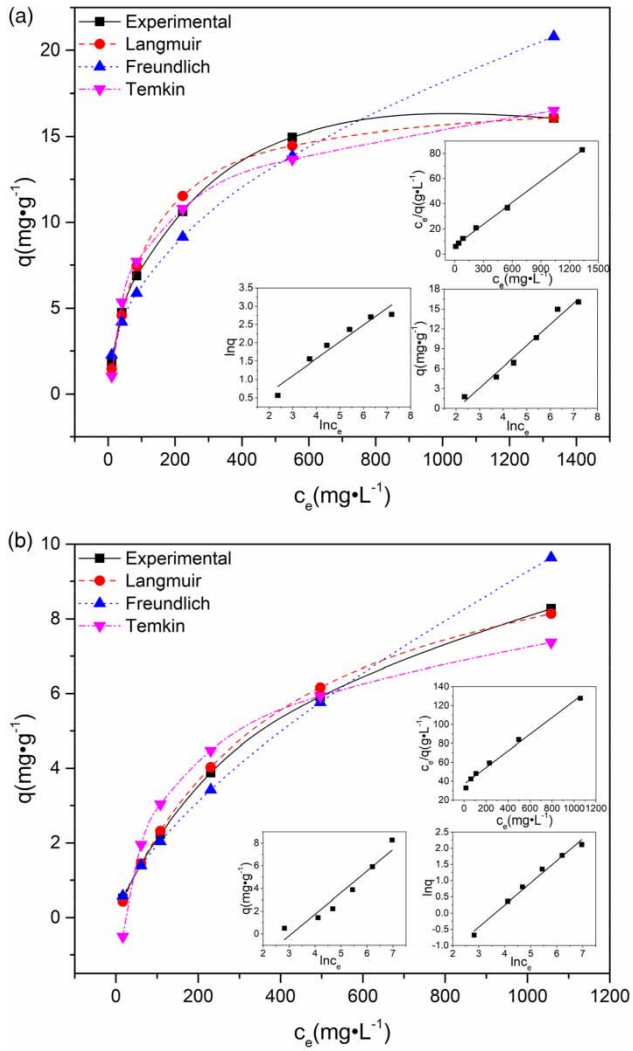

Figure 5 | Adsorption isotherms of nitrogen (a) and phosphorus (b) on the humic acids at 298 K.

Table 2 | Fitting parameters for the adsorption isotherms models calculated from experimental data

	Langmuir			Freundlich			Temkin		
Adsorbates	q_m (mg•g^{-1})	K_L (L•mg^{-1})	R^2	K_F (mg•mg$^{1/n}$)	n	R^2	A	B	R^2
N	17.483	0.0087	0.998	0.763	2.176	0.944	0.130	3.197	0.978
P	11.377	0.0024	0.991	11.820	1.471	0.988	0.046	1.901	0.928

The Temkin isotherm is as follows (Temkin & Pyzhev 1940):

$$q_e = B\ln A + B\ln C_e \quad (7)$$

where A (L•mg^{-1}) is the Temkin isotherm energy constant and B is the Temkin isotherm constant. The corresponding parameters of the Temkin isotherm were obtained from the intercept and slope values of the plot of q_e versus $\ln C_e$.

The HA adsorption isotherms of nitrogen and phosphorus are shown in Figure 5 and the corresponding isotherm model parameters are summarized in Table 2. Langmuir, Freundlich, and Temkin isotherms all fit the data well with high correlation coefficients ($R^2 > 0.9$). However, the Langmuir isotherm model is more suitable for urea-N and phosphate-P adsorption onto HAs than the other models, illustrating that the adsorption process is monomolecular (Zhu *et al.* 2018). Furthermore, the Langmuir isotherm model indicates that the primary adsorption mechanism between the HAs and adsorbate (urea-N and phosphate-P) is monolayer adsorption. (He *et al.* 2017). This result agrees with the FTIR analysis. The maximum adsorption capacity of urea-N and phosphate-P on the HAs calculated from the Langmuir isotherm model is 17.483 mg•g^{-1} and 11.377 mg•g^{-1}, respectively. Based on the aforementioned results, the HAs show promising potential for the adsorption of nitrogen and phosphorus.

Thermodynamic parameters

Thermodynamic experiments of urea-N and phosphate-P adsorption on the HAs were conducted at different temperatures (288, 298, 308, and 318 K) (Figure 6). To further investigate the adsorption process, thermodynamic adsorption parameters including the standard Gibbs free energy change (ΔG°, kJ•mol^{-1}), enthalpy change (ΔH°, kJ•mol^{-1}), and entropy change (ΔS°, kJ•mol^{-1}•K^{-1}) were determined by the following equations:

$$\Delta G^\circ = -RT\ln K_L^\circ \quad (8)$$

$$\Delta G^\circ = \Delta H^\circ - T\Delta S^\circ \quad (9)$$

$$\ln K_L = \frac{\Delta S^\circ}{R} - \frac{\Delta H^\circ}{RT} \quad (10)$$

where R (8.314 J•mol^{-1}•K^{-1}) is the gas constant, T (K) is the absolute temperature, and K_L (L•mol^{-1}) is the Langmuir equilibrium constant. The values of ΔH° and ΔS° can be calculated from the plot of $\ln K_L$ versus 1/T (Figure 6 inset).

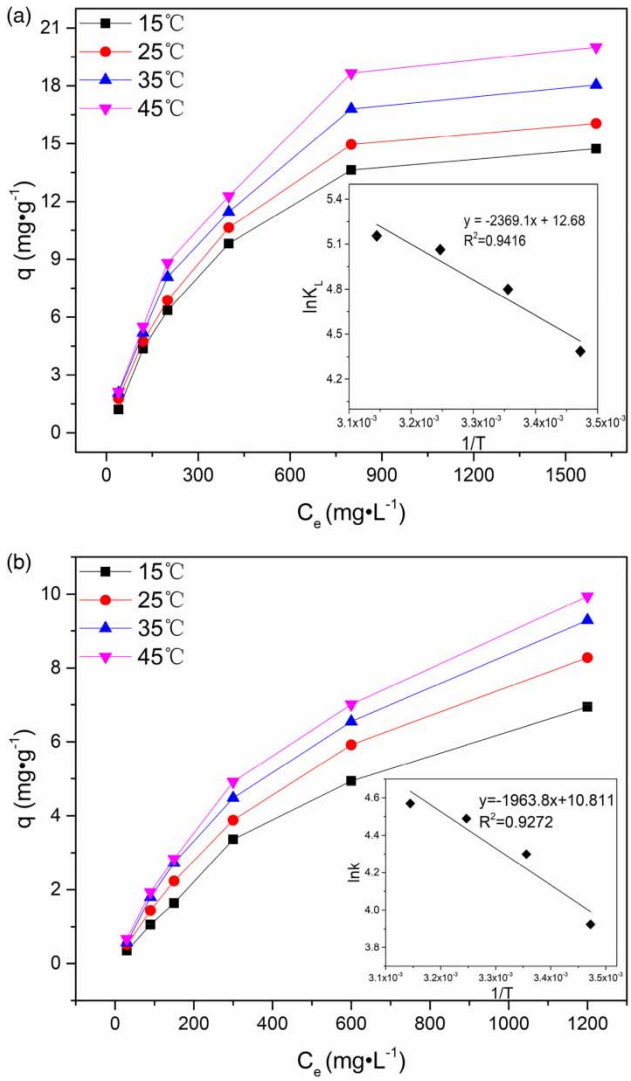

Figure 6 | Effect of temperature on nitrogen (a) and phosphorus (b) adsorption capacity.

Table 3 | Thermodynamic parameters for the adsorption of N and P on humic acids

Adsorbates	Temperature (K)	q_m(mg•g^{-1})	K_L(L•mol^{-1})	R^2	ΔG° (kJ•mol^{-1})	ΔH° (kJ•mol^{-1})	ΔS° (kJ•mol^{-1}•K^{-1})
N	288	16.835	80.317	0.992	−10.502	19.697	0.105
	298	17.483	121.387	0.998	−11.890		
	308	19.231	158.020	0.996	−12.964		
	318	21.231	173.094	0.995	−13.626		
P	288	10.917	50.615	0.988	−9.396	16.327	0.090
	298	11.377	73.670	0.991	−10.653		
	308	12.063	89.056	0.988	−11.496		
	318	12.771	96.519	0.983	−12.082		

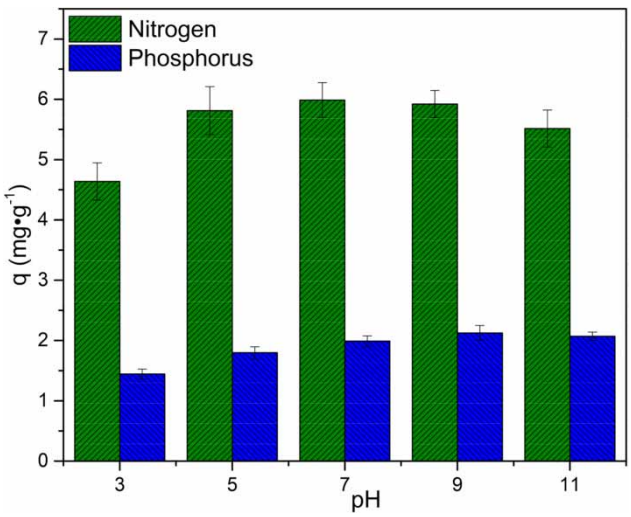

Figure 7 | Effect of initial pH on nitrogen and phosphorus adsorption by the HAs.

The Langmuir equilibrium constant and the adsorption capacity at different temperatures are shown in Table 3. The adsorption rate is enhanced approximately two-fold and the adsorption capacity also clearly increases when the temperature increases from 288 K to 318 K. As shown in Table 3, the values of ΔG° for nitrogen and phosphorus adsorption on HAs are all negative, which indicates that the adsorption process can be spontaneous (Amer & Awwad 2018; Chen *et al.* 2019). The positive ΔH° values imply that both nitrogen and phosphorus adsorption are endothermic processes and favored at higher temperature (Dos Santos *et al.* 2019). In addition, the positive ΔS° values indicate the affinity of the HAs for nitrogen and phosphorus and the increased disorder at the solid-liquid interface (Liao *et al.* 2013).

Effect of initial pH on adsorption

The pH of the solution affects the surface charge of the HAs and the degree of ionization of urea-N and phosphate-P (Sun *et al.* 2017). The effects of initial pH on the nitrogen and phosphorus adsorption capacity by the HAs are shown in Figure 7. Within the pH range from 3 to 11, the adsorption of nitrogen clearly increases with increasing pH from 3 to 5 then varies insignificantly at pH 5–9 before decreasing under alkaline conditions at pH 11. The adsorption of phosphate increases gradually with increasing pH value from 3 to 9 then exhibits a slight decrease with further increases in pH from 9 to 11. However, nitrogen and phosphorus adsorption capacity on the HAs is extremely low at a low pH of 3. This phenomenon is due to the decrease of dissociated carboxyl groups on the surface of HAs at low pH. Furthermore, the reduction in nitrogen and phosphate absorption at pH 11 may be because the electrostatic repulsion between the deprotonated surface of HAs and highly negatively charged phosphate anions is enhanced at alkaline pH (He *et al.* 2017).

CONCLUSIONS

This study analyzed the mechanism of nitrogen and phosphorus adsorption by HAs. Firstly, XRD and SEM-EDS analyses indicated that the HAs predominantly contained organic compounds and kaolinite and FTIR results revealed the presence of abundant functional groups on HAs. Secondly, the effects of initial concentration of pollutant, temperature, and initial pH on the adsorption process were determined by batch experiments. Pseudo-first-order, pseudo-second-order, Elovich, and Weber and Morris intra-particle diffusion kinetic models were used to fit the kinetic data of nitrogen and phosphorus on HAs. Langmuir, Freundlich, and Temkin isotherm models were used to investigate the equilibrium characteristics. The kinetic adsorption process of nitrogen and phosphorus matched well with the pseudo-second-order kinetic model and Weber and Morris intra-particle diffusion kinetic model,

respectively. The Langmuir isotherm model fitted well with both the adsorption isotherm data of nitrogen and phosphorus. Negative ΔG° values and positive ΔH° values indicated that the adsorption process was spontaneous and endothermic. Therefore, the HAs showed substantial potential as an efficient adsorbent for the removal of nitrogen and phosphorus from wastewater.

ACKNOWLEDGEMENTS

This work was supported by the National Science and Technology Pillar Program of China (No. 2015BAD05B03) and the Follow-up Research Project of the Three Gorges Project (No. 2015HXKY2-4).

REFERENCES

Amer, M. W. & Awwad, A. M. 2018 Removal of As(V) from aqueous solution by adsorption onto nanocrystalline kaolinite: equilibrium and thermodynamic aspects of adsorption. *Environmental Nanotechnology, Monitoring & Management* **9**, 37–41.

Canellas, L. P., Olivares, F. L., Aguiar, N. O., Jones, D. L., Nebbioso, A., Mazzei, P. & Piccolo, A. 2015 Humic and fulvic acids as biostimulants in horticulture. *Scientia Horticulturae* **196**, 15–27.

Chen, S., Qin, C., Wang, T., Chen, F., Li, X., Hou, H. & Zhou, M. 2019 Study on the adsorption of dyestuffs with different properties by sludge-rice husk biochar: adsorption capacity, isotherm, kinetic, thermodynamics and mechanism. *Journal of Molecular Liquids* **285**, 62–74.

Derylo-Marczewska, A., Blachnio, M., Marczewski, A. W., Seczkowska, M. & Tarasiuk, B. 2019 Phenoxyacid pesticide adsorption on activated carbon – equilibrium and kinetics. *Chemosphere* **214**, 349–360.

Dodd, R. J. & Sharpley, A. N. 2015 Recognizing the role of soil organic phosphorus in soil fertility and water quality. *Resources, Conservation and Recycling* **105**, 282–293.

Dos Santos, J. M. N., Pereira, C. R., Foletto, E. L. & Dotto, G. L. 2019 Alternative synthesis for $ZnFe_2O_4$/chitosan magnetic particles to remove diclofenac from water by adsorption. *International Journal of Biological Macromolecules* **131**, 301–308.

Freundlich, H. 1906 Uber die adsorption in lasungen. *Journal of Physical Chemistry* **57**, 385–470.

He, Y., Lin, H., Dong, Y. & Wang, L. 2017 Preferable adsorption of phosphate using lanthanum-incorporated porous zeolite: characteristics and mechanism. *Applied Surface Science* **426**, 995–1004.

Huang, J., Xu, C., Ridoutt, B. G., Wang, X. & Ren, P. 2017 Nitrogen and phosphorus losses and eutrophication potential associated with fertilizer application to cropland in China. *Journal of Cleaner Production* **159**, 171–179.

Ji, X. D., Zhang, M. L., Ke, Y. Y. & Song, Y. C. 2013 Simultaneous immobilization of ammonium and phosphate from aqueous solution using zeolites synthesized from fly ashes. *Water Science and Technology* **67** (6), 1324–1331.

Konggidinata, M. I., Chao, B., Lian, Q., Subramaniam, R., Zappi, M. & Gang, D. D. 2017 Equilibrium, kinetic and thermodynamic studies for adsorption of BTEX onto Ordered Mesoporous Carbon (OMC). *Journal of Hazardous Materials* **336**, 249–259.

Krumins, J., Yang, Z., Zhang, Q., Yan, M. & Klavins, M. 2017 A study of weathered coal spectroscopic properties. *Energy Procedia* **128**, 51–58.

Kuśmierek, K., Zarębska, K. & Świątkowski, A. 2016 Hard coal as a potential low-cost adsorbent for removal of 4-chlorophenol from water. *Water Science and Technology* **73** (8), 2025–2030.

Lagergren, S. 1898 About the theory of so-called adsorption of soluble substances. *Kungliga Svenska Vetenskapsakademiens Handlingar* **24**, 1–39.

Langmuir, I. 1918 The adsorption of gases on plane surfaces of glass, mica and platinum. *Journal of the American Chemical Society* **40** (9), 1361–1403.

Leon, A. & Kohyama, K. 2017 Estimating nitrogen and phosphorus losses from lowland paddy rice fields during cropping seasons and its application for life cycle assessment. *Journal of Cleaner Production* **164**, 963–979.

Liao, P., Yuan, S., Xie, W., Zhang, W., Tong, M. & Wang, K. 2013 Adsorption of nitrogen-heterocyclic compounds on bamboo charcoal: kinetics, thermodynamics, and microwave regeneration. *Journal of Colloid and Interface Science* **390** (1), 189–195.

Liu, J., Wang, N., Zhang, H. & Baeyens, J. 2019 Adsorption of Congo red dye on Fe_xCo_3-xO_4 nanoparticles. *Journal of Environmental Management* **238**, 473–483.

Ma, X., Li, Y., Li, B., Han, W., Liu, D. & Gan, X. 2016 Nitrogen and phosphorus losses by runoff erosion: field data monitored under natural rainfall in Three Gorges Reservoir Area, China. *CATENA* **147**, 797–808.

Ma, H., Qiao, Y., Pedersen, C. M., Wang, P., Wu, M., Liu, P., Hou, X., Hu, T. & Wang, Y. 2018 The interaction between Fischer–Tropsch wastewater and humic acid: a NMR study of butanol isomers. *Fuel Processing Technology* **179**, 296–301.

Misra, A. J., Das, S., Habeeb Rahman, A. P., Das, B., Jayabalan, R., Behera, S. K., Suar, M., Tamhankar, A. J., Mishra, A., Lundborg, C. S. & Tripathy, S. K. 2018 Doped ZnO nanoparticles impregnated on Kaolinite (Clay): a reusable nanocomposite for photocatalytic disinfection of multidrug resistant *Enterobacter* sp. under visible light. *Journal of Colloid and Interface Science* **530**, 610–623.

Qian, J., Shen, M., Wang, P., Wang, C., Hu, J., Hou, J., Ao, Y., Zheng, H., Li, K. & Liu, J. 2017 Co-adsorption of perfluorooctane sulfonate and phosphate on boehmite: influence of temperature, phosphate initial concentration and pH. *Ecotoxicology and Environmental Safety* **137**, 71–77.

Qie, L., Yao, Z., Li, G., Xie, S., Yang, Q. & Qi, J. 2018 Equilibrium, kinetics and thermodynamics of Cu(II) biosorption on Chinese chestnut shell pretreated with steam explosion. *Water Science and Technology* **78** (4), 868–877.

Shaker, M. A. & Albishri, H. M. 2014 Dynamics and thermodynamics of toxic metals adsorption onto soil-extracted humic acid. *Chemosphere* **111**, 587–595.

Sun, Z., Yao, G., Liu, M. & Zheng, S. 2017 In situ synthesis of magnetic $MnFe_2O_4$/diatomite nanocomposite adsorbent and its efficient removal of cationic dyes. *Journal of the Taiwan Institute of Chemical Engineers* **71**, 501–509.

Temkin, M. I. & Pyzhev, V. M. 1940 Kinetic of ammonia synthesis on promoted iron catalyst. *Acta Physiochimica URSS* **12**, 327–356.

Uğurlu, M. & Karaoğlu, M. H. 2011 Adsorption of ammonium from an aqueous solution by fly ash and sepiolite: isotherm, kinetic and thermodynamic analysis. *Microporous and Mesoporous Materials* **139** (1–3), 173–178.

Wang, H., Feng, Q. & Liu, K. 2016 The dissolution behavior and mechanism of kaolinite in alkali-acid leaching process. *Applied Clay Science* **132–133**, 273–280.

Wang, Y., Zhu, Y., Zhang, S. & Wang, Y. 2018 What could promote farmers to replace chemical fertilizers with organic fertilizers? *Journal of Cleaner Production* **199**, 882–890.

Weber, W. J. & Morris, J. C. 1963 Kinetics of adsorption on carbon from solution. *Journal of the Sanitary Engineering Division by American Society of Civil Engineers* **89**, 31–60.

Yang, Y., Gao, B., Hao, H., Zhou, H. & Lu, J. 2017 Nitrogen and phosphorus in sediments in China: a national-scale assessment and review. *Science of The Total Environment* **576**, 840–849.

Zhang, Q., Zhao, L., Dong, Y. & Huang, G. 2012 Sorption of norfloxacin onto humic acid extracted from weathered coal. *Journal of Environmental Management* **102**, 165–172.

Zhang, S., Yuan, L., Li, W., Lin, Z., Li, Y., Hu, S. & Zhao, B. 2017 Characterization of pH-fractionated humic acids derived from Chinese weathered coal. *Chemosphere* **166**, 334–342.

Zhang, M., Yao, Y., Tian, Y., Ceng, K., Zhao, M., Zhao, M. & Yin, B. 2018a Increasing yield and N use efficiency with organic fertilizer in Chinese intensive rice cropping systems. *Field Crops Research* **227**, 102–109.

Zhang, Y., Li, Y., Ning, Y., Liu, D., Tang, P., Yang, Z., Lu, Y. & Wang, X. 2018b Adsorption and desorption of uranium(VI) onto humic acids derived from uranium-enriched lignites. *Water Science and Technology* **77** (4), 920–930.

Zhang, S., Yuan, L., Li, W., Lin, Z., Li, Y., Hu, S. & Zhao, B. 2019 Effects of urea enhanced with different weathered coal-derived humic acid components on maize yield and fate of fertilizer nitrogen. *Journal of Integrative Agriculture* **18** (3), 656–666.

Zhao, J., Ni, T., Li, J., Lu, Q., Fang, Z., Huang, Q., Zhang, R., Li, R., Shen, B. & Shen, Q. 2016 Effects of organic–inorganic compound fertilizer with reduced chemical fertilizer application on crop yields, soil biological activity and bacterial community structure in a rice–wheat cropping system. *Applied Soil Ecology* **99**, 1–12.

Zhu, H., Xiao, X., Guo, Z., Han, X., Liang, Y., Zhang, Y. & Zhou, C. 2018 Adsorption of vanadium (V) on natural kaolinite and montmorillonite: characteristics and mechanism. *Applied Clay Science* **161**, 310–316.

First received 28 February 2019; accepted in revised form 13 June 2019. Available online 25 June 2019